

# **Gold(I)-Bisulfite Complexation in Hydrothermal Nanodroplets: A Molecular Dynamics Study**

Wallace C. H. Hui<sup>a</sup> and Kono H. Lemke<sup>a\*</sup>

<sup>a</sup>Department of Earth Sciences, University of Hong Kong, Pokfulam Road, Hong Kong SAR

\*Corresponding author

Email: kono@hku.hk; Tel.: +852-2241-5474; Fax.:+852-2517-6912 (Kono H. Lemke)

A manuscript submitted to *Geochimica et Cosmochimica Acta*

## Abstract

Water nanodroplets present a unique environment for gold hydrothermal transport, with fluid properties in aqueous nanodroplets distinct from bulk liquid and vapor phases. By performing classical and *ab initio* molecular dynamics simulations, we have probed the stability of water nanodroplets  $(\text{H}_2\text{O})_n$  ( $n = 100, 1000$ ) at 25°C and 100°C. The solvation and complexation of gold(I)-bisulfite  $\text{AuHSO}_3$  in nanodroplet environments were also examined, with a particular focus on surface and interior solvation. Classical TIP4P/2005 molecular dynamics simulations reveal extreme densities in the interior of  $(\text{H}_2\text{O})_{100}$  and  $(\text{H}_2\text{O})_{1000}$  nanodroplets compared to droplet surface regions. At 25°C, the interior region of  $(\text{H}_2\text{O})_{100}$  exhibits fluctuating densities at 1.016-1.079 g/cm<sup>3</sup>, with two maxima at 1.079 g/cm<sup>3</sup> and 1.074 g/cm<sup>3</sup>, corresponding to pressures of ~2.23 kbar and 2.07 kbar, respectively; Reduced densities are predicted for the larger  $(\text{H}_2\text{O})_{1000}$  systems, these being 1.013 g/cm<sup>3</sup> (25°C, 370 bar) and 0.968 g/cm<sup>3</sup> (100°C, 220 bar). The outer regions, on the other hand, featured densities intermediate between saturated liquid and vapor conditions, as part of a transition from liquid to vapor-like densities at the edge of the droplet.

Born-Oppenheimer molecular dynamics simulations at 100°C show that the gold(I)-bisulfite complex  $\text{H}_2\text{O-AuHSO}_3$  maintains a near linear solvation structure ( $\theta_{\text{O-Au-S}} = 172^\circ\text{-}174^\circ$ ) in bulk aqueous fluids and at surface and interior sites of  $(\text{H}_2\text{O})_{100}$  nanodroplets. Distance constrained simulations reveal that, upon extension of the gold(I)-bisulfite Au-S contact (equilibrium  $r_{\text{Au-S}} = 2.3$  Å),  $\text{HSO}_3^-$  is displaced by a water molecule, forming a two-water solvation shell around  $\text{Au}^+$ . Thermodynamic integration gives gold(I)-bisulfite dissociation energies ( $\Delta G$ ) of  $17.65 \pm 0.37$  kcal/mol (bulk),  $20.22 \pm 0.38$  kcal/mol (nanodroplet surface), and  $18.31 \pm 0.31$  kcal/mol (nanodroplet interior). Our *ab initio* molecular dynamics results demonstrate that water nanodroplets are stable at hydrothermal conditions and would play an important role in the speciation and transport of gold in volcanic and hydrothermal vapors.

**Keywords**

Vapor phase transport

Nanodroplets

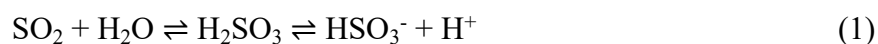
Gold complexation

Molecular dynamics

Thermodynamic integration

## 1. Introduction

Hydrothermal water vapor plays a critical role in the speciation and transport of metals (Lemke and Seward, 2018; Henley and Seward, 2018), and this feature is particularly important in the case of gold due to its well-known affinity for the vapor phase (Archibald *et al.*, 2001; Heinrich *et al.*, 2004; Williams-Jones and Heinrich, 2005; Zevin *et al.*, 2011; Hurtig and Williams-Jones, 2014). The vapor phase, in particular its dense form, is generally understood to lack a continuous network, exhibiting densities and pressures quite distinct from those in the hydrogen-bonded liquid phase. However, the solvation of gold (in the form of  $\text{Au}^+$ ) in dense water vapor, where water clustering or even nanodroplet formation may occur, remains relatively unexplored. Understanding the speciation of gold in the vapor phase involves a detailed examination of the molecular interactions between  $\text{Au}^+$  ions and various sulfur ligands with established binding affinities for gold. Similar to the more well-known bisulfide ion  $\text{HS}^-$  (Seward, 1973; Renders and Seward, 1989; Benning and Seward, 1996; Stefánsson and Seward, 2004; Liu *et al.*, 2011; Williams-Jones *et al.*, 2009; Liu *et al.*, 2014; Brugger *et al.*, 2016), the bisulfite ion  $\text{HSO}_3^-$  and the fully deprotonated sulfite ion  $\text{SO}_3^{2-}$ , which are part of the intermediate sulfur species (ISS), are also possible ligands for  $\text{Au}^+$  complexation in hydrothermal fluids (Benedetti and Boulegue, 1991). Generally, bisulfite ions arise from the interaction between sulfur dioxide and water:



The dissolution of  $\text{SO}_2$  in  $\text{H}_2\text{O}$  gives rise to sulfurous acid  $\text{H}_2\text{SO}_3$ , and at solution  $\text{pH} > 1.88$  (Beyad *et al.*, 2014),  $\text{H}_2\text{SO}_3$  deprotonates and yields the charged bisulfite ion species  $\text{HSO}_3^-$ . Given the abundance of  $\text{SO}_2$  in volcanic and hydrothermal environments (Oppenheimer, 1996; Oppenheimer *et al.*, 1998; Edmonds *et al.*, 2003), examining the stabilities and hydration behaviour of gold-bisulfite complexes is important in understanding the hydrothermal chemistry of gold.

In this study, we explore the structure and stability of the gold-bisulfite complex in high temperature aqueous fluids with a particular focus on gas-phase water clusters and nanodroplets. We present new structural and thermodynamic data for the solvated  $\text{AuHSO}_3$  complex, and these have been derived from *ab initio* molecular dynamics simulations at 100°C. This temperature aligns closely with those observed for gold-bearing fumarolic emissions on White Island, New Zealand (Mandon, 2017). In addition to bulk solvation, we have also examined for the first time the energetic and structural properties of the gold-bisulfite complex in and on the surface of water nanodroplets. It has been previously shown that nonequilibrium water clustering reactions give rise to small nanodroplets consisting of up to 1000 water molecules (Zakharov *et al.*, 1997; Factorovich *et al.*, 2014; Zhong *et al.*, 2017; Nandi *et al.*, 2017; Shima *et al.*, 2024), with noticeable density discontinuities across droplet surface and interior regions (Malek *et al.*, 2018a). Experiments based on optical measurements in diffusion cloud chambers demonstrated water nucleation at near supersaturation conditions up to 100°C (Brus *et al.*, 2008; Brus *et al.*, 2009; Skripov *et al.*, 2023), with nanodroplets in the 100-1000  $\text{H}_2\text{O}$  size range serving as nuclei for aggregation towards larger micron-sized water droplets. Water nanodroplets exhibit a set of unusual physical properties, that differ significantly from those in bulk liquid and even more from the gas phase: for instance, molecular dynamics studies (Zakharov *et al.*, 1997; Factorovich *et al.*, 2014; Malek *et al.*, 2018a) have shown that these densities can range from dense liquids to less dense vapor type environments, but also exhibiting intermediate densities between the conventional saturated liquid and vapor over nanometre size ranges. These nanodroplet systems are anticipated to play an important role in low-density water vapors in volcanic and hydrothermal vent systems, where rapid temperature and pressure fluctuations facilitate disequilibrium nanodroplet formation. These water nanodroplet systems present potential solvation sites for metal ions and metal ion complexes, in particular, in the interior and surface regions. This study aims to probe the structure and thermodynamic properties of the  $\text{AuHSO}_3$  complex across a range of solvation settings, i.e. nanodroplet interior and surface sites, in addition to the bulk liquid

phase. Building on our understanding of the structure of  $\text{AuHSO}_3$  and the nature of its interaction with water droplet sites, we have employed the technique of thermodynamic integration to probe the energetics of complexation and hydration behaviour at nanodroplet interior and surface sites. This approach allows for the estimation of forces and energies involved in bisulfite association with gold(I), the effect of temperature on the complexation constant, and the influence of nanodroplet solvation conditions on the gold-bisulfite complexation reaction.

## 2. Molecular simulation methods

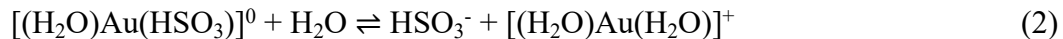
Molecular dynamics simulations were first performed for nanodroplets consisting of 100 and 1000 waters based on the TIP4P/2005 Lennard-Jones-Coulomb potential (Abascal and Vega, 2005), at 25°C and 100°C using the LAMMPS code (Thompson *et al.*, 2022). Simulations for  $(\text{H}_2\text{O})_{100}$  and  $(\text{H}_2\text{O})_{1000}$  were performed in cubic simulation boxes with periodic boundary conditions and side lengths of 35 Å and 100 Å, respectively. A Nosé-Hoover thermostat (Nosé, 1984; Hoover, 1985) was employed to maintain the system at target temperatures of 25°C and 100°C over all simulations. Starting configurations for  $(\text{H}_2\text{O})_{100}$  and  $(\text{H}_2\text{O})_{1000}$  were generated using the artificial bee colony optimizer embedded in the ABCluster software (Zhang & Dolg, 2015, 2016) based on the TIP4P/2005 potential. Each nanodroplet simulation was equilibrated for an initial 0.5 ns period, followed by production simulations of 2 ns at 1.0 fs timesteps. A cutoff distance of 10.0 Å was applied for Lennard-Jones and Coulombic interactions, while long-range electrostatic interactions were calculated using the particle-particle particle-mesh (PPPM) solver optimized for TIP4P water. Simulation trajectories were analysed using the TRAVIS analyzer (Brehm and Kirchner, 2011; Brehm *et al.*, 2020) to obtain density profiles and cluster distributions.

In order to explore the solvation of gold(I)-bisulfite in aqueous media, Born-Oppenheimer molecular dynamics (BOMD) simulations have been undertaken using the QUICKSTEP module of the CP2K code (Kühne *et al.*, 2020). Molecular dynamics simulations employed the generalized-

gradient approximation (GGA) Becke-Lee-Yang-Parr (BLYP) exchange-correlation functional (Becke, 1988; Lee *et al.*, 1988), coupled with the Grimme dispersion correction (BLYP-D3) to account for dispersion interactions (Grimme *et al.*, 2010); core electrons were treated using the Goedecker-Teter-Hutter (GTH) norm-conserving pseudopotentials (Goedecker *et al.*, 1996; Hartwigsen *et al.*, 1998; Krack, 2005), in combination with Gaussian DZVP basis sets (VandeVondele and Hutter, 2007), and auxiliary plane waves with cutoff at 400 Ry. The Nosé-Hoover thermostat was utilized for temperature control (Nosé, 1984; Hoover, 1985).

Periodic boundary conditions have been applied in all three dimensions within the cubic simulation cell, which included a single AuHSO<sub>3</sub> complex and 100 water molecules, and these were configured using the Packmol package (Martínez *et al.*, 2009). Bulk liquid simulations at 100°C (0.958 g/cm<sup>3</sup>) used cubic cells with side dimensions of 14.88 Å. Nanodroplet simulations at 100°C, employed cubic cells with 35 Å side lengths, ensuring sufficient separation to prevent interactions between the primary droplet and its periodic images. Similar box dimensions were adopted in a previous study of SO<sub>2</sub>(H<sub>2</sub>O)<sub>n</sub> nanodroplets with  $n=24-191$  (Zhong *et al.*, 2017). Production simulations were carried out for ~15 ps at 100°C for the following systems: *i*) AuHSO<sub>3</sub> in bulk water, *ii*) AuHSO<sub>3</sub> positioned within the interior of an aqueous nanodroplet, and *iii*) AuHSO<sub>3</sub> located at the nanodroplet surface. A timestep at 1.0 fs was chosen, consistent with previous (H<sub>2</sub>O)<sub>n</sub> nanodroplet BOMD studies (Zhong *et al.*, 2017; Yang *et al.*, 2019; Hadizadeh *et al.*, 2021; Tang and Li, 2022) of similar water numbers ( $n = 32 - 191$ ) that employed the same timestep. Following these production simulations, a series of distance constraint simulations were undertaken for AuHSO<sub>3</sub> in all three solvation settings, where Au-S distances in the gold-bisulfite complex were systematically varied up to the dissociation limit. These constraint calculations serve as the basis for the thermodynamic integration technique (Trout and Parrinello, 1998; Sprik and Ciccotti, 1998). The goal of these calculations is to estimate the free energy changes ( $\Delta G$ ) for the complexation reaction of HSO<sub>3</sub><sup>-</sup> with

$\text{Au}^+$  followed by the (re)attachment of a water molecule onto gold(I), which can be summarized by the following ligand substitution reaction:



In all three solvation environments, distance constraint simulations were first performed with the Au-S distance ( $r_{\text{Au-S}}$ ) fixed at its equilibrium distance of 2.30 Å. Values of  $r_{\text{Au-S}}$  were then systematically increased by intervals of 0.10-0.20 Å, until  $r_{\text{Au-S}}$  approached a value of 4.50 Å. In each constraint simulation step, time-averaged constraint forces were calculated over simulation periods up to 10 ps, after an initial 0.5 ps of equilibration. These time-averaged forces were then integrated with respect to  $r_{\text{Au-S}}$  distances from 2.30 Å to 4.50 Å, to yield values of  $\Delta G$ :

$$\Delta G = - \int F(r_{\text{Au-S}}) dr_{\text{Au-S}} \quad (3)$$

This method facilitates the estimation for free energy change of the reaction outlined in equation (2), in both bulk and nanodroplet solvation settings. The statistical errors on time-averaged forces were estimated with the block averaging method, which accounts for correlation in successive simulation frames in a larger time series (Rodinger *et al.*, 2005; Allen and Tildesley, 2017; Mei *et al.*, 2018); this error estimation technique has been successfully applied in recent metal-ligand constraint simulations (Guan *et al.*, 2022; Guan *et al.*, 2023). Errors in free energies were estimated by applying standard error propagation rules to the integration of individual forces.

### 3. Results and Discussions

#### 3.1. Densities and solvent environments of $(\text{H}_2\text{O})_n$ nanodroplets



Two prototype nanodroplets  $(\text{H}_2\text{O})_{100}$  and  $(\text{H}_2\text{O})_{1000}$  were investigated at 25°C and 100°C, in order to evaluate their stability, structure, and density relative to bulk water. For these exploratory calculations, classical simulations were chosen given their ability to handle extended simulation durations (~2 ns), which are impractical for *ab initio* simulations. A preliminary cluster analysis (Fig. 1) shows that at 25°C, free water monomers constitute only 0.04% and 0.03% of the  $(\text{H}_2\text{O})_{100}$  and  $(\text{H}_2\text{O})_{1000}$  systems, respectively, indicating both droplet systems remain fully intact over extended time periods. At 100°C, the water monomer population increase moderately to 2.4% and 1.0%, thus, around 97 and 990  $\text{H}_2\text{O}$  molecules remain in droplet form in the  $(\text{H}_2\text{O})_{100}$  and  $(\text{H}_2\text{O})_{1000}$  systems, respectively. These results underscore the thermal stability of water nanodroplets, even at the boiling point of water, with larger droplets exhibiting slightly greater stability.

Figure 2 presents the radial density profiles  $\rho(r)$  and running coordination number  $n(r)$  for  $(\text{H}_2\text{O})_{100}$  and  $(\text{H}_2\text{O})_{1000}$  at 25°C and 100°C, calculated as a function of distance from the nanodroplet centre of mass (COM), using the TRAVIS analyzer (Brehm and Kirchner, 2011; Brehm *et al.*, 2020). For the  $(\text{H}_2\text{O})_{100}$  system, the interior region ( $r \leq 6.5$  Å) displays higher densities than at ambient conditions, with notable local density maxima. A steep density decline is observed at 0-1.5 Å, however, as noted by Malek *et al.* (2018a), densities at  $r < 2$  Å are prone to large errors;  $\rho(r)$  integrates to less than 2  $\text{H}_2\text{O}$  in these small volumes, rendering these data points statistically less representative. At 2.0 Å - 6.5 Å, the density  $\rho(r)$  fluctuates between 1.016 g/cm<sup>3</sup> and 1.074 g/cm<sup>3</sup>, averaging at 1.050 g/cm<sup>3</sup>, which is 5% higher than the ambient density of water at 25°C (1 g/cm<sup>3</sup>). This observed density anomaly in the droplet interior region corresponds to a fluid pressure of approximately 1300 bar, suggesting solution conditions characteristic of deep ocean environments. The conversion of fluid densities to pressures was done via the Wagner and Pruß (2002) equation of state of water, confirming the accuracy with the TIP4P/2005 water model. Deviations between measured and calculated water identities were small, at around 0.0007 g/cm<sup>3</sup> at temperatures up to 100°C (Abascal and Vega, 2005). Figure 2 shows two major density anomalies at 3.75 Å and 6.50 Å, with densities of 1.079 g/cm<sup>3</sup> and

1.074 g/cm<sup>3</sup>, corresponding to pressures of around 2200 bar and 2050 bar, respectively, a sub-peak at 2.25 Å with a density of 1.053 g/cm<sup>3</sup> (~1400 bar) is also observed. These distinct peaks align with previous classical MD (based on the mW water model) nanodroplet density profiles at 25°C (Factorovich *et al.*, 2014), albeit for a slightly smaller droplet size (94 H<sub>2</sub>O). Additionally, a density “trough” (1.016 g/cm<sup>3</sup>) is observed at 5.00 Å, corresponding to a fluid pressure of around 440 bar. An inspection of the running coordination number  $n(r)$  reveals that, the first 6.5 Å from the droplet centre comprises 40 water molecules, indicating a 4:6 ratio between interior and surface water molecules. The heightened density and peaks in the droplet interior region at 25°C, are due to the restructuring of water molecules and the additional pressure from surface tension induced by the curved droplet surface (Malek *et al.*, 2018b). Beyond 6.5 Å, the density profile steadily decreases, approaching zero at ~11 Å, which marks the droplet/vacuum boundary. This density decline at the droplet surface region also aligns with findings from previous MD studies of water droplets (Zakharov *et al.*, 1997; Factorovich *et al.*, 2014; Malek *et al.*, 2018a), and is the result of fewer neighbouring surface waters, resulting in weaker intermolecular interactions and a less dense packing of H<sub>2</sub>O in this region. Densities at the outer region, i.e. 7.25 Å - 11.0 Å, are intermediate between the saturated liquid density at 25°C (0.997 g/cm<sup>3</sup>) and vapor density (2x10<sup>-5</sup> g/cm<sup>3</sup>). This feature suggests a gradual transition from dense high-pressure liquid-like conditions to low-pressure, vapor-like environment, in other words, the droplet surface region is in a stage of preparation for evaporation.

For the (H<sub>2</sub>O)<sub>100</sub> system at 100°C, the density profile at  $r < 5$  Å exhibits diminished fluctuation compared to 25°C. The droplet region covering  $r \approx 2 - 5$  Å demonstrates a near constant density of 0.988 g/cm<sup>3</sup>, corresponding to a fluid pressure of 700 bar at 100°C. Both density and pressure are reduced compared to 25°C (1.050 g/cm<sup>3</sup> and 1333 bar), but remain higher than the saturated liquid conditions at 100°C (0.958 g/cm<sup>3</sup> and 1 bar). The running coordination number  $n(r)$  indicates that the interior region ( $r \leq 5.0$  Å) contains around 17 water molecules, resulting in a ~2:8 ratio between interior and surface waters. The density profile  $\rho(r)$  reaches zero at  $r = 14.5$  Å, thus, the outer droplet

region at 100°C spans a larger volume ( $r = 5.0 - 14.5 \text{ \AA}$ ,  $V=12246.4 \text{ \AA}^3$ ). As a result of a higher proportion of water molecules in the surface region (80% at 100°C versus 60% at 25°C), the overall density at 100°C is reduced due to droplet expansion. Overall, these results demonstrate that an increase in temperature from 25°C to 100°C causes *i)* an overall nanodroplet expansion, *ii)* contraction of the interior region with fewer water molecules, *iii)* a significant volume expansion of the outer region of the droplet, and *iv)* reduced densities and pressures in both interior and surface regions.

In the larger  $(\text{H}_2\text{O})_{1000}$  system, density fluctuations are dampened, and overall densities are reduced compared to the smaller  $(\text{H}_2\text{O})_{100}$  droplet, consistent with trends reported in previous classical MD studies (Factorovich *et al.*, 2014). As seen from Figure 2, the  $(\text{H}_2\text{O})_{1000}$  density profile at 25°C peaks at  $3.50 \text{ \AA}$  ( $1.031 \text{ g/cm}^3$ ), with minor peaks at  $7.25 \text{ \AA}$  ( $1.023 \text{ g/cm}^3$ ) and  $13.75 \text{ \AA}$  ( $1.020 \text{ g/cm}^3$ ). These maxima are less pronounced than those in the  $(\text{H}_2\text{O})_{100}$  system ( $1.079 \text{ g/cm}^3$  and  $1.074 \text{ g/cm}^3$ ). The dampened densities relative to the  $(\text{H}_2\text{O})_{100}$  system are likely due to a larger droplet size causing interior region fluid characteristics to trend towards more bulk-like properties. Additionally, the larger droplet volume lessens surface curvature, diminishing the impact of surface tension on the density profile. This leads to a more uniform water distribution and less pronounced density peaks compared to the  $(\text{H}_2\text{O})_{100}$  system. The interior region ( $r \leq 16 \text{ \AA}$ ) of the  $(\text{H}_2\text{O})_{1000}$  nanodroplet at 25°C yields an average density at  $1.013 \text{ g/cm}^3$ , corresponding to a fluid pressure of around 370 bar, which is noticeably lower than that in the smaller  $(\text{H}_2\text{O})_{100}$  system (1330 bar). In the outer region, on the other hand, the reduction in density is more gradual in the  $(\text{H}_2\text{O})_{1000}$  droplet ( $16.0 - 23.0 \text{ \AA}$ ) than in the  $(\text{H}_2\text{O})_{100}$  droplet ( $6.5 - 11.0 \text{ \AA}$ ). This feature is attributed to the larger droplet size and lower surface curvature, which diminishes the effect of surface tension, leading to a smoother transition from dense liquid to vapor-like densities. At 100°C, the  $(\text{H}_2\text{O})_{1000}$  droplet density profile displays a near-constant density trend of  $0.968 \text{ g/cm}^3$  over the range  $r = 2.0 - 14.5 \text{ \AA}$ , corresponding to  $\sim 200$  bar, and this value is just  $\sim 1\%$  larger than the 100°C saturated liquid density ( $0.958 \text{ g/cm}^3$ ). This

suggests that at 100°C, the interior solvent environment in a (H<sub>2</sub>O)<sub>1000</sub> nanodroplet closely resembles that of bulk water. Density decays steadily starting at  $r = 14.5 \text{ \AA}$  and approaches zero at  $r = 25.0 \text{ \AA}$ , thus, an increase in droplet size gives rise to a less structured and more uniform core, with densities trending towards conventional liquid-like conditions. Overall, these classical MD simulation results suggest that high-pressure conditions ( $\geq 1 \text{ kbar}$ ), common in geothermal and hydrothermal systems, can also exist in more dense vapor-like environments, particularly in the inner regions of water nanodroplets. Smaller droplets are characterised by slightly higher pressures, while lower water densities in the surface region of the nanodroplet create an intermediate hydration environment, with densities that fall between those of typical liquids and vapor phases.

We next present results from *ab initio* BOMD simulations of a (H<sub>2</sub>O)<sub>100</sub> nanodroplet at 25°C and 100°C, which serve as a reference for subsequent AuHSO<sub>3</sub> metal complex simulation in (H<sub>2</sub>O)<sub>100</sub>. Briefly, these BOMD simulations demonstrate that (H<sub>2</sub>O)<sub>100</sub> nanodroplets remain structurally intact over  $\sim 30 \text{ ps}$  at 25°C and 100°C. In response to one reviewer, we also undertook a set of exploratory production runs at higher temperatures, i.e. 300°C, to probe the structural integrity of water droplets, without explicitly probing AuHSO<sub>3</sub> complexation reactions within the droplet. These simulations revealed that (H<sub>2</sub>O)<sub>100</sub> nanodroplets undergo rapid initial evaporation before entering into equilibrium with surrounding water molecules. For instance, at 300°C, nanodroplets retained around 80 water molecules at elevated vapor densities ( $0.11 \text{ g/cm}^3$ ) after 30 ps, compared to a slightly smaller nanodroplet with 50 waters in the lower density simulation ( $0.07 \text{ g/cm}^3$ ). These results demonstrate that while higher temperatures accelerate nanodroplet evaporation, this effect can be offset by increasing the water monomer density, allowing for the stabilisation of the nanodroplet in higher-density vapor environments.

Radial density analyses of (H<sub>2</sub>O)<sub>100</sub> (Fig. 3) at 25°C and 100°C reveal that the density profiles  $\rho(r)$  align closely with those derived from our TIP4P/2005 simulations, with densities approaching zero at  $11.0 \text{ \AA}$  (25°C) and  $14.5 \text{ \AA}$  (100°C) from the droplet centre. The 25°C *ab initio* MD profile

shows two major density peaks at 4.50 Å and 6.50 Å, and a sub-peak at 3.75 Å, aligning with the TIP4P/2005 density profile. However, *ab initio* MD density profiles display enhanced fluctuations between 0 – 6.5 Å, particularly near the droplet centre ( $r < 2.0$  Å), which is caused by the shorter duration (30 ps) of the simulation run. Figure 4 presents radial distribution function (RDF)  $g_{O-O}(r)$  profiles for surface and interior water molecules at both 25°C and 100°C, where we tracked three water molecules consistently in the droplet interior, and three water molecules on the droplet surface. At 25°C, the first  $g_{O-O}$  peak for surface waters is at 2.81 Å, which is further than that for interior waters (2.78 Å), reflecting a diminished surface density compared to droplet interior. This difference between the interior and surface waters is also reflected in the 100°C  $g_{O-O}(r)$  profiles, albeit shifted to longer distances due to the elevated temperature, with surface and interior waters  $g_{O-O}(r)$  peaking at 2.86 Å and 2.79 Å. These results suggest that distinct regions (surface and interior) within a  $(H_2O)_{100}$  nanodroplet exhibit varied densities and pressures, influencing how geochemical species (e.g. sulfur dioxide and sulfites) are solvated and transported in vapor environments. A preliminary conclusion that can be drawn from our *ab initio* MD simulations is that *i*) water nanodroplets exhibit distinct densities mimicking high-density fluid environments, but also those intermediate, between bulk liquid and vapor densities, with a caveat that these droplets exist as liquid-like gas-phase entities; *ii*) this is particularly important for larger droplets (e.g. ~1000 to 10000  $H_2O$ ) in moderate temperature hydrothermal settings, where solute species can partition into distinct droplet solvation regions, characterized by unique water densities and dielectric constant values; and *iii*) these density variations across nanodroplets are also likely to influence inorganic and organic complexation reactions with large volume differences, influencing their speciation in hydrothermal low-density vapors.

### 3.2. Structure and stability of the gold-bisulfite $[Au(HSO_3)]^0$ complex at 100°C

Building on our droplet simulation results, we now examine the effect of droplet structure and hydrogen bonding environment on the complexation behaviour of Au(I) with the bisulfite anion

$\text{HSO}_3^-$ . *Ab initio* MD simulations of the  $\text{AuHSO}_3$  complex at  $100^\circ\text{C}$  were performed in three solvation settings: *i*) bulk aqueous fluid, *ii*) nanodroplet interior, and *iii*) nanodroplet surface, to probe the structure and stability of the gold-bisulfite complex in these distinct settings. In all three solvation settings, the  $\text{Au}^+$  ion is hydrated by 2 water molecules in a linear configuration, consistent with mass spectrometric IRMPD gas-phase and quantum chemical solvation studies (Poisson *et al.*, 2002; Li *et al.*, 2012). Figure 5 depicts this structure in which one of the water molecules has been replaced by the  $\text{HSO}_3^-$  anion with one Au-S bisulfite contact, and an extended Au-O water contact. No ligand exchange reactions were observed throughout the simulation. The time-averaged (15 ps) Au-S distances ( $r_{\text{Au-S}}$ ) in  $\text{AuHSO}_3$  are at  $2.305 \pm 0.056$  Å (bulk),  $2.314 \pm 0.067$  Å (droplet interior), and  $2.309 \pm 0.049$  Å (droplet surface). The close alignment between the three  $r_{\text{Au-S}}$  values suggests that the gold-sulfur distance in  $\text{AuHSO}_3$  is insensitive to the solvation environment. The angle distribution function (ADF) for the O-Au-S angle (see Fig. 5) was estimated from trajectory data, showing an optimal angle at around  $172^\circ$  in the bulk phase,  $174^\circ$  for the droplet interior, and  $172.9^\circ$  for the droplet surface. These values are notably smaller than the *ab initio* MD based  $180^\circ$  angle reported for the  $\text{H}_2\text{O-Au}^+\text{-OH}_2$  solvation complex (Camellone and Marx, 2012); this feature can be attributed to charge-transfer processes taking place between the S atom (electron donation and backdonation) and  $\text{Au}^+$ , resulting in an overall stabilisation and softening of the interaction as the bonding shifts from being predominantly ionic (as in the case of  $\text{H}_2\text{O-Au}^+\text{-OH}_2$ ) to one with enhanced covalent character due to electron sharing in  $\text{H}_2\text{O-Au}^+\text{-HSO}_3^-$ .

Expanding on these structural insights for the  $\text{H}_2\text{O-Au}^+\text{-HSO}_3^-$  complex, we present  $\Delta G$  estimates for the gold-bisulfite-water ligand substitution reaction at  $100^\circ\text{C}$  (given in Eq. 2), derived from thermodynamic integration techniques. Constrained *ab initio* MD simulations were conducted by incrementally extending Au-S distances; forces captured at each constraint step were integrated with respect to Au-S distances, yielding free energy ( $\Delta G$ ) estimates (see Eq. 3). The resulting Au-S force and energy profiles are presented in Figs. 6 – 7. Uncertainties in forces and errors at each

constraint step are listed in Table S1. First, we describe results from AuHSO<sub>3</sub> constraint simulations in the bulk liquid phase at 100°C. Figure 6 shows negative forces across Au-S distances of  $r = 2.30$  Å - 3.00 Å, indicating attraction forces between Au<sup>+</sup> and HSO<sub>3</sub><sup>-</sup> ions at these separation distances. A maximum in the attraction force profile exists at  $r_{\text{Au-S}} = 2.70$  Å, indicating that the initial stages of HSO<sub>3</sub><sup>-</sup> dissociation from Au<sup>+</sup> involve overcoming significant attractive forces ( $-37.02 \pm 0.99$  kcal/mol·Å). At a separation distance of roughly  $r_{\text{Au-S}} = 3.10$  Å, however, these forces switch to being positive, highlighting a shift from attraction to repulsion between Au<sup>+</sup> ion and the sulfur terminus in HSO<sub>3</sub><sup>-</sup>. This transition also coincides with a water molecule substituting for the bisulfite anion, resulting in an approximately linear coordination for H<sub>2</sub>O-Au<sup>+</sup>-OH<sub>2</sub>. A closer examination of this constraint simulation reveals that at  $r_{\text{Au-S}} = 3.00$  Å, a water molecule approaches the Au<sup>+</sup> ion and positions itself at an oblique angle to the linear O-Au-S arrangement. This gives rise to a reduction in the attractive forces between Au and S to  $-24.21 \pm 0.54$  kcal/mol·Å. At a distance  $r_{\text{Au-S}}$  of 3.10 Å, the Au<sup>+</sup> ion then forms a new linear H<sub>2</sub>O-Au<sup>+</sup>-OH<sub>2</sub> structure, with Au-O distances of  $2.146 \pm 0.063$  Å and  $2.147 \pm 0.075$  Å, while the bisulfite ion undergoes repulsion from Au ( $8.88 \pm 0.66$  kcal/mol·Å). This linear two-water solvation motif around Au<sup>+</sup> agrees with results from IRMPD spectroscopy (Poisson *et al.*, 2002; Li *et al.*, 2012) and Car-Parrinello molecular dynamics simulations (Camellone and Marx, 2012). The two water solvation structure remains stable as  $r_{\text{Au-S}}$  increases to 3.70 Å, where Au-S interaction diminishes to 0 kcal/mol·Å, indicating that the Au<sup>+</sup> and HSO<sub>3</sub><sup>-</sup> interactions at these separation distances are minimal. At an Au-S distance of ~4.10 Å, weakly repulsive forces ( $2.13 \pm 0.57$  kcal/mol·Å) develop as the bisulfite ion pivots, positioning an O atom site in proximity to Au<sup>+</sup> (average Au-O distance =  $3.392 \pm 0.229$  Å). This reduced repulsion persists from  $r_{\text{Au-S}} = 3.90$  Å to 4.30 Å, before converging to zero and reaching equilibrium at 4.50 Å. At the constrained distance  $r_{\text{Au-S}} = 4.50$  Å, HSO<sub>3</sub><sup>-</sup> is coordinated by 7 H<sub>2</sub>O, with an optimal S-O distance of 3.85 Å (Fig. S2), aligning well with that of free HSO<sub>3</sub><sup>-</sup> in solution. This feature underscores that the solvation environment around HSO<sub>3</sub><sup>-</sup> at  $r_{\text{Au-S}} = 4.50$  Å resembles that of a free HSO<sub>3</sub><sup>-</sup>, confirming full



dissociation from  $\text{Au}^+$ . To confirm the existence of equilibrium at  $r_{\text{Au-S}} = 4.50 \text{ \AA}$ , additional constrained simulations were performed at  $r_{\text{Au-S}}$  distances =  $4.80 \text{ \AA}$ ,  $5.10 \text{ \AA}$ ,  $5.40 \text{ \AA}$ . The time-averaged forces at these extended separation distances were estimated as  $-0.36 \pm 0.69 \text{ kcal/mol}\cdot\text{\AA}$  ( $4.80 \text{ \AA}$ ),  $0.37 \pm 0.65 \text{ kcal/mol}\cdot\text{\AA}$  ( $5.10 \text{ \AA}$ ), and  $-0.34 \pm 1.10 \text{ kcal/mol}\cdot\text{\AA}$  ( $5.40 \text{ \AA}$ ). These small force values underscore that  $\text{Au}^+$  and  $\text{HSO}_3^-$  are sufficiently separated at  $r_{\text{Au-S}} = 4.50 \text{ \AA}$ , and integrating forces for  $r_{\text{Au-S}} > 4.50 \text{ \AA}$  would have negligible impact on the free energy estimate.

Next, we examine the thermodynamic properties of the  $\text{AuHSO}_3$  complex on the surface and within the interior of a nanodroplet with 100 water molecules (Fig. 7). Throughout the dissociation of  $\text{AuHSO}_3$  on the water droplet surface ( $r_{\text{Au-S}} = 2.3 \text{ \AA} - 4.5 \text{ \AA}$ ),  $\text{Au}^+$  and  $\text{HSO}_3^-$  are positioned beyond  $6.3 \text{ \AA}$  from the droplet COM. In contrast, for the interior solvation environment, both ions remain within  $3.9 \text{ \AA}$  of the COM (Fig. S3). This highlights that  $\text{Au}^+$  and  $\text{HSO}_3^-$  remain at the droplet surface throughout dissociation without crossing over to the interior region. As seen from Fig. 7, maxima in the Au-S force profile (at  $r_{\text{Au-S}} = 2.70 \text{ \AA}$ ) are calculated to be  $-40.01 \pm 0.91 \text{ kcal/mol}\cdot\text{\AA}$  and  $-38.26 \pm 0.94 \text{ kcal/mol}\cdot\text{\AA}$  for droplet surface and interior sites, respectively. Interestingly, these values are both moderately stronger than that calculated for the bulk aqueous phase ( $-37.02 \pm 0.99 \text{ kcal/mol}\cdot\text{\AA}$ ). In other words, larger forces are required to overcome the attraction between  $\text{Au}^+$  and  $\text{HSO}_3^-$  within nanodroplet solvation settings, and in particular, at the droplet surface versus bulk phase; subsequently, forces transition towards repulsion, and reach maxima at  $r_{\text{Au-S}} = 3.10 \text{ \AA}$ , at  $7.68 \pm 0.74 \text{ kcal/mol}\cdot\text{\AA}$  (surface) and  $7.95 \pm 0.56 \text{ kcal/mol}\cdot\text{\AA}$  (interior). Consistent with  $\text{AuHSO}_3$  constraint simulations in bulk liquid water, the shift towards repulsion at  $r_{\text{Au-S}} \approx 3.10 \text{ \AA}$  is caused by the substitution of bisulfite ion with a  $\text{H}_2\text{O}$  molecule, resulting in a linear solvated gold di-aquo complex, i.e.  $\text{H}_2\text{O-Au}^+-\text{OH}_2$ . In both nanodroplet solvation environments, forces converge to  $\sim 0$  at  $r_{\text{Au-S}} = 3.70 \text{ \AA}$ , with minor fluctuations around zero forces between  $3.70 \text{ \AA} - 4.50 \text{ \AA}$ , implying that, in the cases of droplet interior and surface solvation settings, force data points beyond  $r_{\text{Au-S}} = 3.70 \text{ \AA}$  would have negligible influence on free energy estimates. Additional constrained simulations at extended  $r_{\text{Au-S}}$



distances (4.80, 5.10, 5.40 Å) yielded near-zero time-averaged forces for both surface and interior solvation (surface:  $-0.34 \pm 0.99$ ,  $0.38 \pm 0.70$ ,  $0.70 \pm 0.77$  kcal/mol·Å; interior:  $-0.24 \pm 0.63$ ,  $-0.55 \pm 0.72$ ,  $-0.41 \pm 0.94$  kcal/mol·Å), thus confirming sufficient force convergence at  $r_{\text{Au-S}} = 4.50$  Å.

The integration of AuHSO<sub>3</sub> constraint force data points across all three solvation environments (bulk liquid, droplet surface, interior) are then used to determine values of  $\Delta G$  at 100°C for the gold-bisulfite-water substitution reaction (Eq. 2). These  $\Delta G$  estimates provide insight into the stability of AuHSO<sub>3</sub> across these settings, helping to distinguish between *i*) liquid versus both *ii,iii*) droplet speciation scenarios of the AuHSO<sub>3</sub> ion complex. For AuHSO<sub>3</sub> in aqueous solution *i*), the calculated  $\Delta G$  for complex dissociation according to eq. 2 is  $17.65 \pm 0.37$  kcal/mol, implying that the dissociation of this ion complex and water substitution to H<sub>2</sub>O-Au<sup>+</sup>-OH<sub>2</sub> is unfavourable at 100°C. Thermodynamic integration up to an extended separation distance of  $r_{\text{Au-S}} = 5.40$  Å yields a comparable  $\Delta G$  value of  $17.78 \pm 0.47$  kcal/mol, indicating that integration up to 4.50 Å is sufficient in order to capture the total free energy change  $\Delta G$  for AuHSO<sub>3</sub> dissociation.

For AuHSO<sub>3</sub> in the (H<sub>2</sub>O)<sub>100</sub> nanodroplet interior *ii*), the calculated  $\Delta G$  value is  $18.31 \pm 0.31$  kcal/mol. The close alignment between  $\Delta G$  values for bulk liquid and nanodroplet interior environments (difference  $\sim 0.66$  kcal/mol), suggests that, despite the elevated pressure ( $\sim 1$  kbar) within the nanodroplet interior, the solvated AuHSO<sub>3</sub> ion complex retains bulk-like stability characteristics. For AuHSO<sub>3</sub> at the droplet surface *iii*), force integration yields  $\Delta G = 20.22 \pm 0.38$  kcal/mol, which is considerably larger than that in the interior or in bulk solution. This suggests that the free energy of dissociation for AuHSO<sub>3</sub> to free Au<sup>+</sup> and HSO<sub>3</sub><sup>-</sup> on the droplet surface is moderately larger, by only  $\sim 2$  kcal/mol, compared to the droplet interior. These *ab initio* MD results indicate that the AuHSO<sub>3</sub> complex is more stable on the water nanodroplet surface than in the interior region or in bulk fluid settings. Thus, in a nanodroplet environment, the AuHSO<sub>3</sub> complex is more likely to remain intact, and more importantly, would partition towards the surface rather than reside in the interior region of the nanodroplet. A detailed examination of the force profiles shows that the larger  $\Delta G$  value

for nanodroplet surface solvation (i.e. enhanced  $\text{AuHSO}_3$  stability), results from the stronger attractive (i.e. negative) forces during the initial phase of  $\text{AuHSO}_3$  dissociation. Specifically, at  $r_{\text{Au-S}} = 2.70\text{-}3.00$  Å, forces calculated for  $\text{AuHSO}_3$  surface solvation are on average  $2.76$  kcal/mol·Å stronger than those in the droplet interior and bulk fluid. This results in a larger free energy requirement for  $\text{AuHSO}_3$  dissociation at the nanodroplet surface. The enhanced stability of  $\text{AuHSO}_3$  at the nanodroplet surface is also due to the incomplete solvation water network, and in particular, the absence of a full solvation shell around  $\text{AuHSO}_3$  that would otherwise stabilise the separated  $\text{Au}^+$  and  $\text{HSO}_3^-$  ions.

### 3.3. Geochemical implications

**Figure 8** summarises calculated densities for  $(\text{H}_2\text{O})_n$  nanodroplets ( $n=100,1000$ ) at  $25^\circ\text{C}$  and  $100^\circ\text{C}$ , derived from AIMD and TIP4P/2005 classical simulations, alongside reported fluid densities for droplets with  $n = 94\text{-}960$  at  $25^\circ\text{C}$  and  $45^\circ\text{C}$  (classical MD, [Factorovich \*et al.\*, 2014](#)). As seen, nanodroplet interior regions exhibit higher fluid densities (by  $0.01 - 0.1$  g/cm<sup>3</sup>) across  $25^\circ\text{C} - 100^\circ\text{C}$ ; surface regions, on the other hand, are characterised by an outward transition in densities, spanning liquid ( $\rho > 0.95$  g/cm<sup>3</sup>), to super-saturated vapor ( $0.0006$  g/cm<sup>3</sup>  $< \rho < 0.95$  g/cm<sup>3</sup>), to vapor ( $\rho < 0.0006$  g/cm<sup>3</sup>) densities at the droplet boundary. These results imply that in dense volcanic vapors, gold-bisulfite and related complexes are solvated within and on nanodroplets of various sizes each with characteristic solvent densities. This solvation behaviour is driven primarily by *i*) the size of the water nanodroplet itself and, more importantly, *ii*) by the choice of solvation site within and on the droplet moiety. Thus, nanodroplets not only host different solvation sites for molecular ions, but also serve as important transporting agents, enhancing the mobility of gold in the vapor phase due to their high buoyancy. This aspect is particularly relevant for volcanic systems with high water vapor content and elevated gold concentrations. For instance, the White Island hydrothermal systems host fumaroles with temperatures ranging from  $60^\circ\text{C}$  to  $750^\circ\text{C}$ , with the Noisy Neille fumaroles vent system at

around 100°C (Mandon, 2017), closely matching the conditions covered in this study. Fumarolic gases on White Island consist primarily of water vapor (~90 mol%), with small amounts of SO<sub>2</sub> (~1%), and gold (~0.05 µg Au/kg H<sub>2</sub>O at 0.09 kg/day) (Mandon *et al.*, 2019; Mandon *et al.*, 2020). As heated vapors rapidly ascend and cool, nanodroplet nucleation is anticipated to occur, consistent with experimental water nucleation studies (Brus *et al.*, 2008); the resulting nanodroplet size and the corresponding solvation behaviour are directly influenced by the cooling rate and water vapor pressure. For instance, with vapor emission rates at the White Island Volcano of up to 50-100 kg/s (Rose *et al.*, 1986) and nanodroplet nucleation rates of the order of 10<sup>-1</sup> to 10<sup>2</sup>/cm<sup>3</sup> s (Brus *et al.*, 2008), this process is estimated to produce around 10<sup>4</sup> to 10<sup>7</sup> water nanodroplets/m<sup>3</sup>·s. Finally, the droplet-surface enhanced complexation of AuHSO<sub>3</sub> can also contribute towards the formation of gold-bisulfite clusters in the vapor-phase of fumarolic gas systems. Of particular interest here is the formation of larger polynuclear gold bisulfite complexes at droplet surface sites, where dielectric constant values are reduced. These polynuclear complexes could then conceivably serve as early prenucleation species during gold-bisulfite precipitation within and on water nanodroplets.

#### 4. Conclusions

We have studied the stability of the AuHSO<sub>3</sub> ion complex in bulk hydrothermal and nanodroplet environments. These *ab initio* molecular dynamic simulations have yielded new insights into the structure of high-temperature water nanodroplets, the complexation and hydration behavior of AuHSO<sub>3</sub> in bulk solution and water nanodroplets, and the ability of AuHSO<sub>3</sub> to partition between surface and interior regions within water nanodroplets. First, results from classical MD simulation at 25°C and 100°C reveal that the interior region of (H<sub>2</sub>O)<sub>100</sub> nanodroplets maintain a compact hydrogen-bonding network with densities ranging up to 1.05 g/cm<sup>3</sup> and pressures reaching up to 1.3 kbar. In contrast, the water nanodroplet surface exhibits a low-density, vapor-like hydrogen-bonding network with intermediate densities between liquid water (0.958 g/cm<sup>3</sup>) and water vapor (0.0006

g/cm<sup>3</sup>) at 100°C. In other words, nanodroplets with 100-1000 water molecules can function as gas-phase species, while retaining both bulk and vapor-like density characteristics, and featuring surface solvation sites that strongly influence the complexation and hydration behavior of AuHSO<sub>3</sub>. Results from *ab initio* MD simulations at 100°C highlight that the mono-hydrated gold-bisulfite complex (H<sub>2</sub>O)AuHSO<sub>3</sub> maintains a near-linear solvation structure with  $\theta_{\text{O-Au-S}}=172\text{-}174^\circ$ , both in bulk fluid settings, and in water nanodroplets such as (H<sub>2</sub>O)<sub>100</sub>. Thermodynamic integration of constraint forces yields AuHSO<sub>3</sub> dissociation energy values ( $\Delta G$  at 100°C) of  $18.31 \pm 0.31$  kcal/mol and  $20.22 \pm 0.38$  kcal/mol, compared to  $17.65 \pm 0.37$  kcal/mol in bulk fluid. The close similarity between  $\Delta G$  values in the nanodroplet interior and bulk liquid, indicates that the hydrogen-bonding environment in the water droplet interior closely resembles that of the bulk fluid. However, transfer of the AuHSO<sub>3</sub> ion complex from the droplet interior to its surface environment results in a small but nevertheless noticeable enhancement in the association of AuHSO<sub>3</sub>, favouring the transfer of bisulfite ions to near-surface regions in preparation for gold complexation.

## Acknowledgements

This exploratory study is the culmination of countless conversations with Terry, starting at the ETH and later during Terry's frequent visits to HKU, about the nature of steam, water clusters, and nanodroplets, and the need for us to probe these phases in more detail to understand metal behaviour in vapor. Terry was the first to seriously investigate complexation and solvation in water clusters and nanodroplets, using what was then a relatively unknown technique to geochemists, high-pressure mass spectrometry. We feel that this small study on gold complexation in nanodroplets honours this goal and represents a natural progression of some of Terry's ideas, concepts, and also his enthusiasm for quantum chemical simulations. It gives us tremendous joy to imagine how Terry would have reacted to this work, and how he might have responded to the peculiar behaviour of gold in water nanodroplets.

This work was supported by the HK General Research Fund HKU (Grant No. P17330216, P17307118, and P17308120) and computing time provided to K.H.L. and W.C.H.H. by the HKU High Performance Computing (Grant No. HPC2021) Center.

## CRediT authorship statement

**Wallace C. H. Hui:** Writing – original draft. **Kono H. Lemke:** Writing – original draft.

**Data availability**

Data are available through Mendeley Data at <https://doi.org/10.17632/45zmsbxzny.3>

Journal Pre-proofs

**Appendix A. Supplementary Material**

Supplementary figures illustrating the temporal evolution of nanodroplet evaporation at 300°C (Fig. S1), the RDF for water oxygen around sulfur (in  $\text{HSO}_3^-$ ) with distant  $\text{Au}^+$  ( $r_{\text{Au-S}} = 4.5 \text{ \AA}$ ) compared to free  $\text{HSO}_3^-$  in bulk solvation (Fig. S2), the position of  $\text{AuHSO}_3$  with respect to  $(\text{H}_2\text{O})_{100}$  center of mass (COM) in surface and interior constrained simulations (Fig. S3), and a supplementary table listing calculated force and energies, including associated uncertainties, at each  $r_{\text{Au-S}}$  constraint step for bulk liquid, nanodroplet surface, and interior solvation environments (Table S1).

## References

- Abascal, J. L., Vega, C., 2005. A general purpose model for the condensed phases of water: TIP4P/2005. *The J. Chem. Phys.* 123, 234505.
- Allen, M. P., Tildesley, D. J., 2017. *Computer simulation of liquids*. Oxford University Press.
- Archibald, S. M., Migdisov, A. A., Williams-Jones, A. E., 2001. The stability of Au-chloride complexes in water vapor at elevated temperatures and pressures. *Geochim. Cosmochim. Acta* 65, 4413-4423.
- Becke, A. D., 1988. Density-functional exchange-energy approximation with correct asymptotic behavior. *Phys. Rev. A* 38, 3098.
- Benedetti, M., Boulegue, J., 1991. Mechanism of gold transfer and deposition in a supergene environment. *Geochim. Cosmochim. Acta* 55, 1539-1547.
- Benning, L. G., Seward, T. M., 1996. Hydrosulphide complexing of Au(I) in hydrothermal solutions from 150–400°C and 500–1500 bar. *Geochim. Cosmochim. Acta* 60, 1849-1871.
- Beyad, Y., Burns, R., Puxty, G., Maeder, M., 2014. A speciation study of sulfur(IV) in aqueous solution. *Dalton Trans.* 43, 2147-2152.
- Brehm, M., Kirchner, B., 2011. TRAVIS—A Free Analyzer and Visualizer for Monte Carlo and Molecular Dynamics Trajectories. *J. Chem. Inf. Model* 51, 2007-2023.



- Brehm, M., Thomas, M., Gehrke, S., Kirchner, B., 2020. TRAVIS—A free analyzer for trajectories from molecular simulation. *J. Chem. Phys.* 152, 164105.
- Brugger, J., Liu, W., Etschmann, B., Mei, Y., Sherman, D. M., Testemale, D., 2016. A review of the coordination chemistry of hydrothermal systems, or do coordination changes make ore deposits?. *Chem. Geol.* 447, 219-253.
- Brus, D., Ždímal, V., Smolík, J., 2008. Homogeneous nucleation rate measurements in supersaturated water vapor. *J. Chem. Phys.* 129, 174501.
- Brus, D., Ždímal, V., Uchtmann, H., 2009. Homogeneous nucleation rate measurements in supersaturated water vapor II. *J. Chem. Phys.* 131, 074507.
- Camellone, M. F., Marx, D., 2012. Solvation of  $\text{Au}^+$  versus  $\text{Au}^0$  in aqueous solution: electronic structure governs solvation shell patterns. *Phys. Chem. Chem. Phys.* 14, 937-944.
- Edmonds, M., Oppenheimer, C., Pyle, D. M., Herd, R. A., Thompson, G., 2003.  $\text{SO}_2$  emissions from Soufrière Hills Volcano and their relationship to conduit permeability, hydrothermal interaction and degassing regime. *J. Volcanol. Geotherm. Res.* 124, 23-43.
- Factorovich, M. H., Molinero, V., & Scherlis, D. A., 2014. Vapor pressure of water nanodroplets. *J. Am. Chem. Soc.* 136, 4508-4514.
- Goedecker, S., Teter, M., Hutter, J., 1996. Separable dual-space Gaussian pseudopotentials. *Phys. Rev. B* 54, 1703.

- Grimme, S., Antony, J., Ehrlich, S., Krieg, H., 2010. A consistent and accurate ab initio parametrization of density functional dispersion correction (DFT-D) for the 94 elements H-Pu. *J. Chem. Phys.* 132, 154104.
- Guan, Q., Mei, Y., Etschmann, B., Louvel, M., Testemale, D., Bastrakov, E., Brugger, J., 2022. Yttrium speciation in sulfate-rich hydrothermal ore-forming fluids. *Geochim. Cosmochim. Acta* 325, 278-295.
- Guan, Q., Mei, Y., Liu, W., Brugger, J., 2023. Different metal coordination in sub-and super-critical fluids: Do molybdenum(IV) chloride complexes contribute to mass transfer in magmatic systems? *Geochim. Cosmochim. Acta* 354, 240-251.
- Hadizadeh, M. H., Yang, L., Fang, G., Qiu, Z., Li, Z., 2021. The mobility and solvation structure of a hydroxyl radical in a water nanodroplet: a Born–Oppenheimer molecular dynamics study. *Phys. Chem. Chem. Phys.* 23, 14628-14635.
- Hartwigsen, C., Goedecker, S., Hutter, J., 1998. Relativistic separable dual-space Gaussian pseudopotentials from H to Rn. *Phys. Rev. B* 58, 3641.
- Heinrich, C. A., Driesner, T., Stefánsson, A., Seward, T. M., 2004. Magmatic vapor contraction and the transport of gold from the porphyry environment to epithermal ore deposits. *Geology* 32, 761-764.

- Henley, R. W., Seward, T. M., 2018. Gas-Solid reactions in arc volcanoes; ancient and modern. *Rev. Mineral. Geochem.* 84, 309–350.
- Hoover, W. G., 1985. Canonical dynamics: Equilibrium phase-space distributions. *Phys. Rev. A* 31, 1695.
- Hurtig, N. C., Williams-Jones, A. E., 2014. An experimental study of the transport of gold through hydration of AuCl in aqueous vapour and vapour-like fluids. *Geochim. Cosmochim. Acta* 127, 305-325.
- Krack, M., 2005. Pseudopotentials for H to Kr optimized for gradient-corrected exchange-correlation functionals. *Theor. Chem. Acc.* 114, 145-152.
- Kühne, T. D., Iannuzzi, M., Ben, M. D., Rybkin, V. V., Seewald, P., Stein, F., Laino, T., Khaliullin, R. Z., Schütt, O., Schiffmann, F., Golze, D., Wilhelm, J., Chulkov, S., Bani-Hashemian, M. H., Weber, V., Borštnik, U., Taillefumier, M., Jakobovits, A. S., Lazzaro, A., Pabst, H., Müller, T., Schade, R., Guidon, M., Andermatt, S., Holmberg, N., Schenter, G. K., Hehn, A., Bussy, A., Belleflamme, F., Tabacchi, G., Glöß, A., Lass, M., Bethune, I., Mundy, C. J., Plessl, C., Watkins, M., VandeVondele, J., Krack, M., Hutter, J., 2020. CP2K: an electronic structure and molecular dynamics software package – Quickstep: efficient and accurate electronic structure calculations. *J. Chem. Phys.* 152, 194103.
- Lee, C., Yang, W., Parr, R. G., 1988. Development of the Colle-Salvetti correlation-energy formula into a functional of the electron density. *Phys. Rev. B* 37, 785.

- Lemke, K. H., Seward, T. M., 2018. Molecular clusters and solvation in volcanic and hydrothermal vapors. *Rev. Mineral. Geochem.* 84, 57–83.
- Li, Y., Wang, G., Wang, C., Zhou, M., 2012. Coordination and solvation of the  $\text{Au}^+$  cation: infrared photodissociation spectroscopy of mass-selected  $\text{Au}(\text{H}_2\text{O})_n^+$  ( $n = 1-8$ ) complexes. *J. Phys. Chem. A* 116, 10793-10801.
- Liu, W., Etschmann, B., Testemale, D., Hazemann, J. L., Rempel, K., Müller, H., Brugger, J., 2014. Gold transport in hydrothermal fluids: Competition among the  $\text{Cl}^-$ ,  $\text{Br}^-$ ,  $\text{HS}^-$  and  $\text{NH}_3(\text{aq})$  ligands. *Chem. Geol.* 376, 11-19.
- Liu, X., Lu, X., Wang, R., Zhou, H., Xu, S., 2011. Speciation of gold in hydrosulphide-rich ore-forming fluids: Insights from first-principles molecular dynamics simulations. *Geochim. Cosmochim. Acta* 75, 185-194.
- Malek, S. M., Poole, P. H., Saika-Voivod, I., 2018a. Thermodynamic and structural anomalies of water nanodroplets. *Nat. Commun.* 9, 2402.
- Malek, S. M., Sciortino, F., Poole, P. H., Saika-Voivod, I., 2018b. Evaluating the Laplace pressure of water nanodroplets from simulations. *J. Phys. Condens. Matter* 30, 144005.
- Mandon, C., 2017. Volatile Transport of Metals in the Andesitic Magmatic-hydrothermal System of White Island. PhD Thesis. Victoria University of Wellington, Wellington.

- Mandon, C. L., Christenson, B. W., Schipper, C. I., Seward, T. M., Garaebiti, E. 2019, Metal transport in volcanic plumes: a case study at White Island and Yasur volcanoes. *J. Volcanol. Geotherm. Res.* 369, 155-171.
- Mandon, C. L., Seward, T. M., Christenson, B. W. 2020, Volatile transport of metals and the Cu budget of the active White Island magmatic-hydrothermal system, New Zealand. *J. Volcanol. Geotherm. Res.* 398, 106905
- Martínez, L., Andrade, R., Birgin, E. G., Martínez, J. M., 2009. PACKMOL: A package for building initial configurations for molecular dynamics simulations. *J. Comput. Chem.* 30, 2157-2164.
- Mei, Y., Liu, W., Brugger, J., Sherman, D. M., Gale, J. D., 2018. The dissociation mechanism and thermodynamic properties of HCl(aq) in hydrothermal fluids (to 700°C, 60 kbar) by ab initio molecular dynamics simulations. *Geochim. Cosmochim. Acta* 226, 84-106.
- Nandi, P. K., Burnham, C. J., Futera, Z., English, N. J., 2017. Ice-amorphization of supercooled water nanodroplets in no man's land. *ACS Earth Space Chem.* 1, 187-196.
- Nosé, S., 1984. A unified formulation of the constant temperature molecular dynamics methods. *J. Chem. Phys.* 81, 511-519.
- Oppenheimer, C., 1996. On the role of hydrothermal systems in the transfer of volcanic sulfur to the atmosphere. *Geophys. Res. Lett.* 23, 2057-2060.

- Oppenheimer, C., Francis, P., Stix, J., 1998. Depletion rates of sulfur dioxide in tropospheric volcanic plumes. *Geophys. Res. Lett.* 25, 2671-2674.
- Poisson, L., Lepetit, F., Mestdagh, J. M., Visticot, J. P., 2002. Multifragmentation of the  $\text{Au}(\text{H}_2\text{O})_{n \leq 10}^+$  cluster ions by collision with helium. *J. Phys. Chem. A* 106, 5455-5462.
- Renders, P. J., Seward, T. M., 1989. The stability of hydrosulphido- and sulphido-complexes of Au(I) and Ag(I) at 25°C. *Geochim. Cosmochim. Acta* 53, 245-253.
- Rodinger, T., Howell, P. L., Pomès, R., 2005. Absolute free energy calculations by thermodynamic integration in four spatial dimensions. *J. Chem. Phys.* 123, 034104.
- Rose, W. I., Chuan, R. L., Giggenbach, W. F., Kyle, P. R., Symonds, R. B., 1986. Rates of sulfur dioxide and particle emissions from White Island volcano, New Zealand, and an estimate of the total flux of major gaseous species. *Bull. Volcanol.* 48, 181-188.
- Seward, T. M., 1973. Thio complexes of gold and the transport of gold in hydrothermal ore solutions. *Geochim. Cosmochim. Acta* 37, 379-399.
- Shima, N., Harada, Y., Takahashi, O., 2024. Structural analysis of nano-water droplets: A molecular dynamics study. *Chem. Phys. Lett.* 852, 141521.
- Skripov, P. V., Bar-Kohany, T., Antonov, D. V., Strizhak, P. A., Sazhin, S. S., 2023. Approximations for the nucleation temperature of water. *Int. J. Heat Mass Transf.* 207, 123970.

- Sprik, M., Ciccotti, G., 1998. Free energy from constrained molecular dynamics. *J. Chem. Phys.* 109, 7737-7744.
- Stefánsson, A., Seward, T. M., 2004. Gold(I) complexing in aqueous sulphide solutions to 500°C at 500 bar. *Geochim. Cosmochim. Acta* 68, 4121-4143.
- Tang, B., Li, Z., 2022. Mechanisms of Reactions between HOI and HY (Y= Cl, Br, I) on a Water Nanodroplet Surface. *J. Phys. Chem. A* 126, 8028-8036.
- Thompson, A. P., Aktulga, H. M., Berger, R., Bolintineanu, D. S., Brown, W. M., Crozier, P. S., Veld, P. J. I., Kohlmeyer, A, Moore, S. G., Nguyen, T. D., Shan, R., Stevens, M. J., Tranchida, J., Trott, C., Plimpton, S. J., 2022. LAMMPS - a flexible simulation tool for particle-based materials modeling at the atomic, meso, and continuum scales, *Comput. Phys. Commun.* 271, 108171.
- Trout, B. L., Parrinello, M., 1998. The dissociation mechanism of H<sub>2</sub>O in water studied by first-principles molecular dynamics. *Chem. Phys. Lett.* 288, 343–347.
- VandeVondele, J., Hutter, J., 2007. Gaussian basis sets for accurate calculations on molecular systems in gas and condensed phases. *J. Chem. Phys.* 127, 114105.
- Wagner, W., Pruß, A., 2002. The IAPWS formulation 1995 for the thermodynamic properties of ordinary water substance for general and scientific use. *J. Phys. Chem. Ref. Data* 31, 387-535.

- Williams-Jones A. E., Heinrich C. A., 2005. Vapour transport of metals and the formation of magmatic-hydrothermal ore deposits. *Econ. Geol.* 100, 1287–1312.
- Williams-Jones, A. E., Bowell, R. J., Migdisov, A. A., 2009. Gold in solution. *Elements*, 5, 281-287.
- Yang, J., Li, L., Wang, S., Li, H., Francisco, J. S., Zeng, X. C., Gao, Y. 2019. Unraveling a new chemical mechanism of missing sulfate formation in aerosol haze: gaseous NO<sub>2</sub> with aqueous HSO<sub>3</sub><sup>-</sup>/SO<sub>3</sub><sup>2-</sup>. *J. Am. Chem. Soc.* 141, 19312-19320.
- Zakharov, V. V., Brodskaya, E. N., Laaksonen, A., 1997. Surface tension of water droplets: A molecular dynamics study of model and size dependencies. *J. Chem. Phys.* 107, 10675-10683.
- Zein D. Yu., Migdisov A. A., Williams-Jones A. E., 2011. The solubility of gold in H<sub>2</sub>O–H<sub>2</sub>S vapour at elevated temperature and pressure. *Geochim. Cosmochim. Acta.* 75, 5140-5153.
- Zhang, J., Dolg, M. ABCluster: The Artificial Bee Colony Algorithm for Cluster Global Optimization. *Phys. Chem. Chem. Phys.* 2015, 17, 24173-24181.
- Zhang, J., Dolg, M. Global Optimization of Rigid Molecular Clusters by the Artificial Bee Colony Algorithm. *Phys. Chem. Chem. Phys.* 2016, 18, 3003-3010.
- Zhong, J., Zhu, C., Li, L., Richmond, G. L., Francisco, J. S., Zeng, X. C., 2017. Interaction of SO<sub>2</sub> with the Surface of a Water Nanodroplet. *J. Am. Chem. Soc.* 139, 17168-17174.



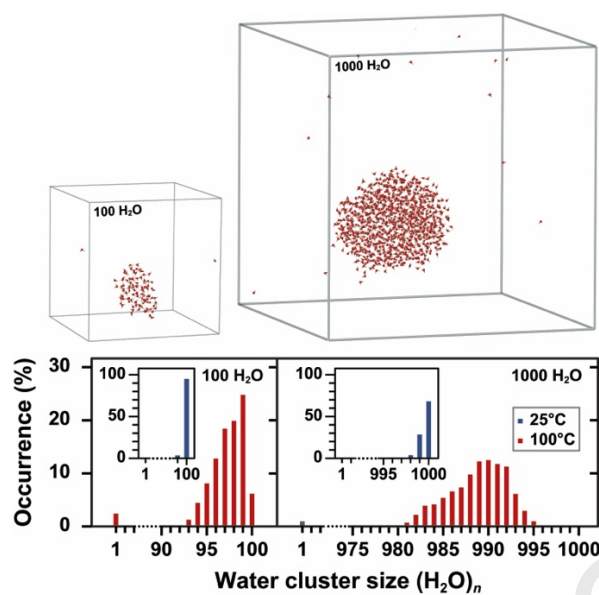


**Fig. 1.** Snapshots of TIP4P/2005 simulation cells containing  $(H_2O)_{100}$  and  $(H_2O)_{1000}$  nanodroplet systems at 100°C (top); cluster analysis of  $(H_2O)_{100}$  and  $(H_2O)_{1000}$  simulations at 100°C, insets illustrate results at 25°C (bottom).

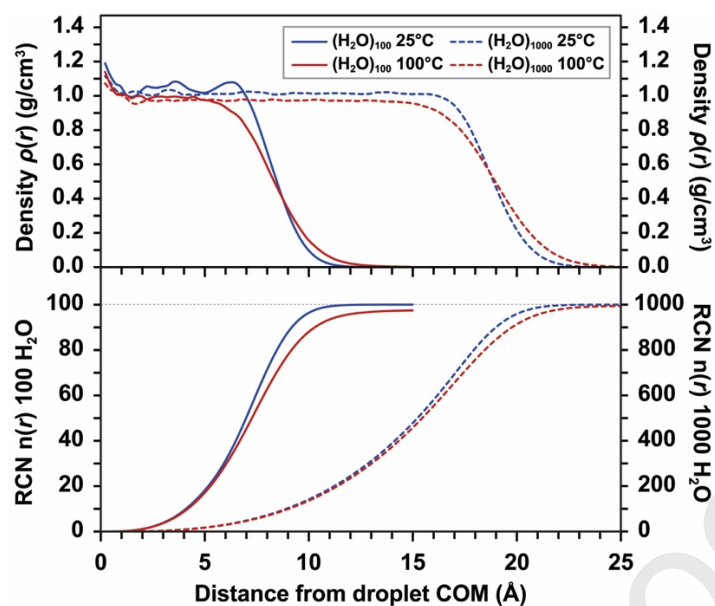


**Fig. 2.** Density profiles  $\rho(r)$  (top) and running coordination numbers  $n(r)$  (bottom) as a function of distance from the droplet centre of mass for  $(\text{H}_2\text{O})_{100}$  and  $(\text{H}_2\text{O})_{1000}$  at 25°C and 100°C, calculated from classical TIP4P/2005 simulations and averaged over 2 ns.

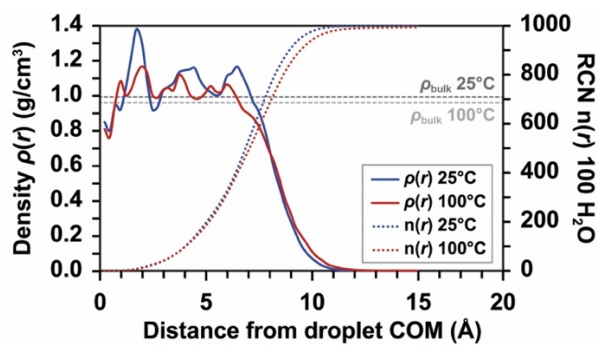


**Fig. 3.** Density profiles  $\rho(r)$  and running coordination number  $n(r)$  as a function of distance from the droplet centre of mass for  $(\text{H}_2\text{O})_{100}$  at 25°C and 100°C, calculated from *ab initio* MD simulations, averaged over 30 ps. Densities of bulk water at 25°C and 100°C are also included for comparison.

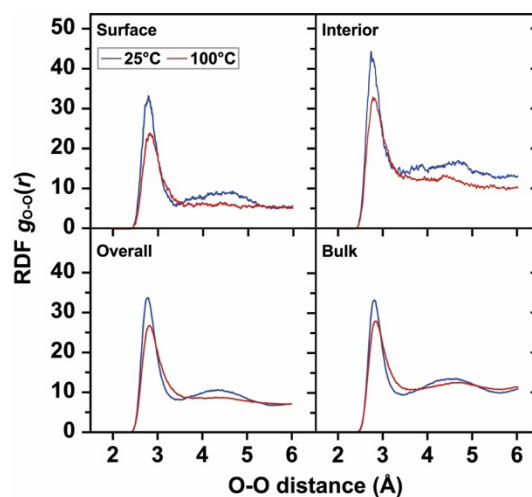


**Fig. 4.** Comparison of oxygen-oxygen radial distribution function  $g_{O-O}(r)$  for surface, interior, and all water molecules in  $(H_2O)_{100}$  nanodroplet, and in bulk water, calculated from *ab initio* MD simulations at 25°C and 100°C.

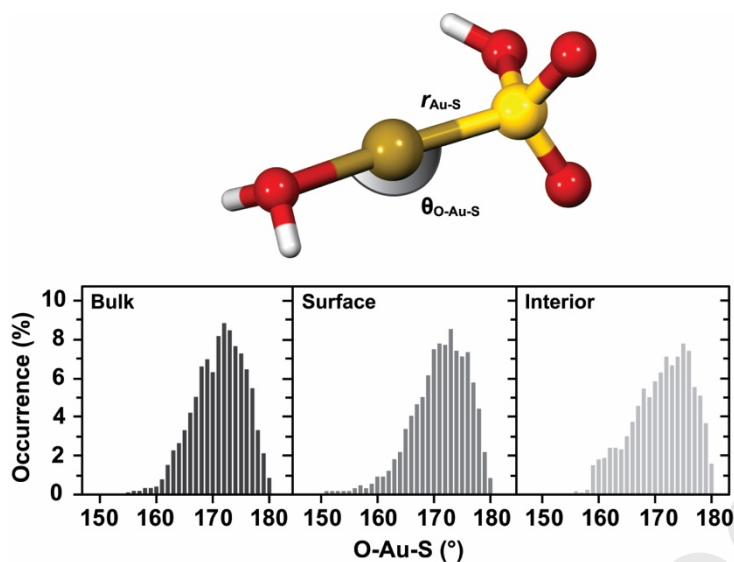


**Fig. 5.** Configuration of the gold(I)-bisulfite complex, coordinated with a single water molecule (top); angle distribution function (ADF) for the oxygen-gold-sulfur angle ( $\theta_{\text{O-Au-S}}$ ) across bulk water, and surface and interior solvation sites in a  $(\text{H}_2\text{O})_{100}$  nanodroplet, derived from 100°C *ab initio* MD simulations (bottom).

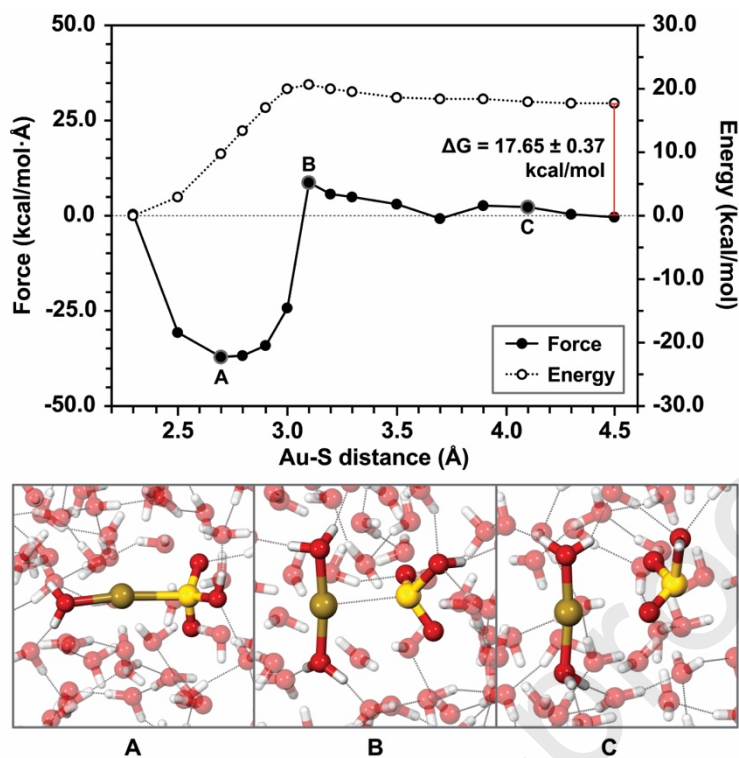


**Fig. 6.** Constraint forces and free energy profile for AuHSO<sub>3</sub> dissociation (equation 2) in bulk solvation at 100°C as a function of Au-S distances (top); snapshots showing stages of AuHSO<sub>3</sub> dissociation at  $r_{\text{Au-S}} = 2.7$  Å (A), 3.1 Å (B), and 4.1 Å (C) (bottom).

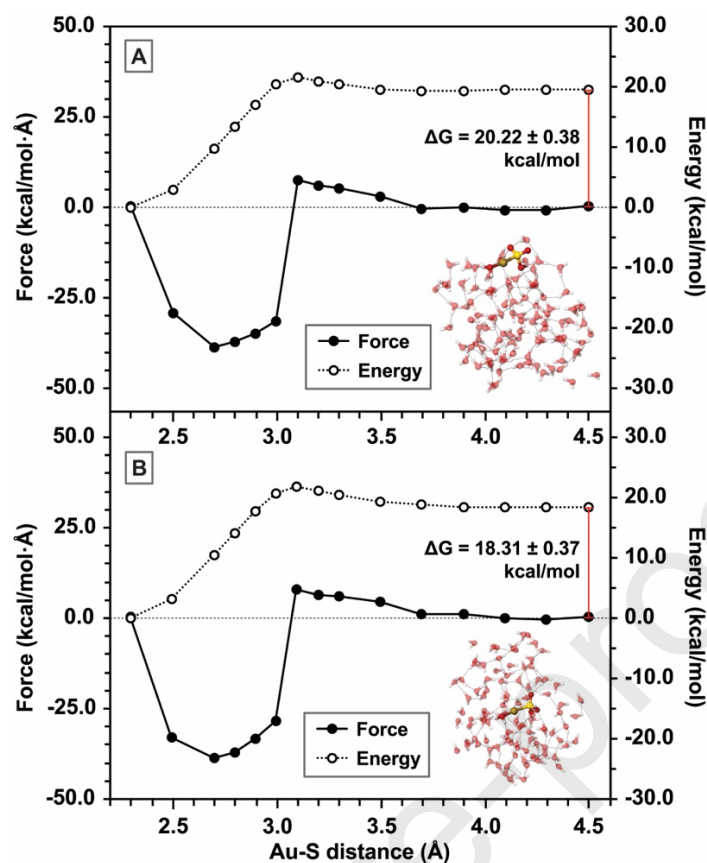


**Fig. 7.** Constraint forces and free energy profile for  $\text{AuHSO}_3$  dissociation (equation 2) in  $(\text{H}_2\text{O})_{100}$  nanodroplet surface (A) and interior (B) solvation at  $100^\circ\text{C}$  as a function of Au-S distances.

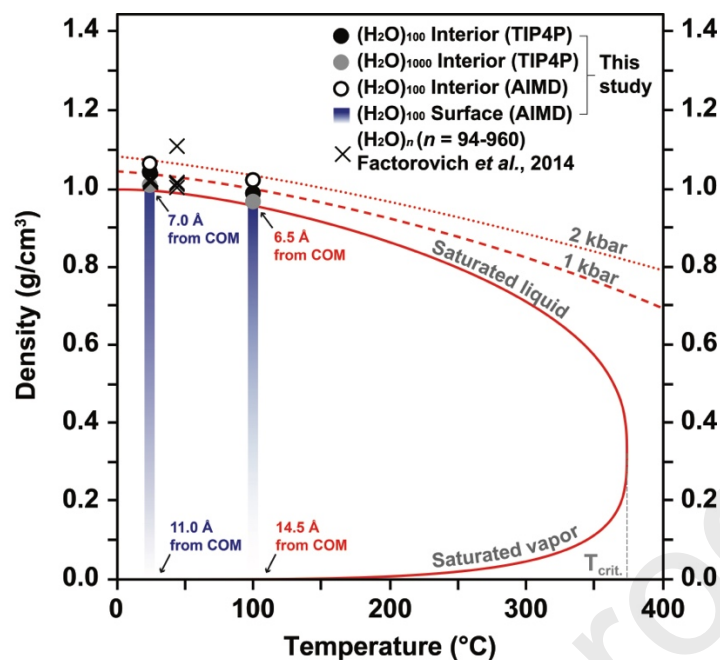


**Fig. 8.** Calculated densities of  $(H_2O)_{100}$  and  $(H_2O)_{1000}$  nanodroplets obtained from AIMD and TIP4P/2005 simulations (this study), reported  $(H_2O)_n$  densities from classical simulations (Factorovich *et al.*, 2014), and compared with conventional liquid and vapor densities. For  $(H_2O)_{100}$  nanodroplets, surface densities derived from AIMD simulations are shown as a gradient from 25°C to 100°C, with the shading intensity indicating proximity to the center of mass (COM).